

Exploring single-molecule dynamics with fluorescence nanoscopy

Christian Ringemann¹, Ben Harke¹, Claas von Middendorff¹,
Rebecca Medda¹, Alf Honigmann², Richard Wagner²,
Marcel Leutenegger¹, Andreas Schönle¹, Stefan W Hell¹
and Christian Eggeling¹

¹ Department of Nanobiophotonics, Max Planck Institute for Biophysical Chemistry, Am Fassberg 11, 37077 Göttingen, Germany

² Biophysik, University Osnabrück, FB Biologie/Chemie, Osnabrück, Germany
E-mail: ceggeli@gwdg.de

New Journal of Physics **11** (2009) 103054 (29pp)

Received 30 April 2009

Published 27 October 2009

Online at <http://www.njp.org/>

doi:10.1088/1367-2630/11/10/103054

Abstract. The study of molecular dynamics at the single-molecule level with fluorescence correlation spectroscopy (FCS) and far-field optics has contributed greatly to the functional understanding of complex systems. Unfortunately, such studies are restricted to length scales of >200 nm because diffraction does not allow further reduction of the measurement volume. This sets an upper limit on the applicable concentration of fluorescently labeled molecules and even more importantly, averages out details of nanoscale dynamics. By combining FCS and fluorescence intensity distribution analysis (FIDA) with sub-diffraction-resolution stimulated emission depletion (STED) nanoscopy, we remove this restriction and obtain open measurement volumes of nanoscale dimensions which are tunable in size. As a consequence, single-molecule studies can now be extended to nanoscale dynamics and may be applied to much larger, often endogenous concentrations. In solution, low-brightness signal from axial out-of-focus volume shells was taken into account by using both FCS and FIDA in conjunction to analyze the data. In two-dimensional systems, such as lipid membranes, the background is greatly reduced and measurements feature excellent signal-to-noise ratios. Measurement foci of down to 30 nm in diameter directly reveal anomalous diffusion of lipids in the plasma membrane of living cells and allow for the determination of on/off rates of the binding of lipids

to other membrane constituents. Such important insight into the prominent biological question of lipid membrane organization or ‘lipid rafts’ shows that combining fluctuation analysis with STED-engineered ultra-small measurement volumes is a viable and powerful new approach to probing molecular dynamics on the nanoscale.

Contents

| | |
|--|-----------|
| 1. Introduction | 2 |
| 2. Experimental | 4 |
| 2.1. Dye solution | 4 |
| 2.2. Multilamellar layer | 4 |
| 2.3. Horizontal black lipid bilayer | 5 |
| 2.4. Cellular membrane | 5 |
| 2.5. STED microscope | 5 |
| 2.6. FCS | 7 |
| 2.7. FIDA | 8 |
| 2.8. Apparent particle number and brightness | 9 |
| 2.9. FIDA correction | 10 |
| 2.10. FCS analysis of lipid membrane diffusion | 11 |
| 2.11. Monte Carlo simulation of lipid membrane diffusion | 12 |
| 3. Results and discussion | 12 |
| 3.1. Principle of STED nanoscopy | 12 |
| 3.2. Aqueous environment | 13 |
| 3.3. Dependence on experimental conditions | 17 |
| 3.4. Suppression of low-brightness signal contributions | 20 |
| 3.5. STED–FCS on lipid membranes | 21 |
| 3.6. Photobleaching | 23 |
| 3.7. Live cell observations | 24 |
| 4. Conclusion | 26 |
| Acknowledgments | 27 |
| Appendix. Global FCS–FIDA analysis | 27 |
| References | 28 |

1. Introduction

The study of cellular processes requires sensitive and non-invasive observation techniques. Using visible light, fluorescence microscopy is largely benign to biological tissue and has reached a sensitivity that allows for the detection of single molecules with high temporal resolution. It is thus ideally suited to study cellular dynamics on the molecular level and quantitative analysis of such single-molecule experiments is readily performed by studying the fluctuations of the fluorescence signal using well-established techniques like fluorescence correlation spectroscopy (FCS) [1]–[3] and photon-counting histogram (PCH) analysis [4] or fluorescence intensity distribution analysis (FIDA) [5]. However, due to the diffraction of light, far-field optics cannot separate the signal from features of the same kind that are less than

approximately half the wavelength apart, i.e. 200–250 nm when using visible light [6]. This limited resolution blocks further insights into a lot of important biophysical processes because (i) it sets a lower limit on the achievable measurement volume and (ii) with sizes of <20 nm the molecular building blocks of complex systems such as proteins are still out of reach. As a consequence, the concentration of fluorescently marked molecules in single-molecule studies has to be in the nanomolar range, which is sometimes below the natural and endogenous concentration of the molecules under study, making it essential to lower the volume's scale below diffraction [7, 8]. More importantly, the standard confocal microscopy spot usually averages over details of nanoscale molecular dynamics. It has been demonstrated that some information about nanoscopic movement can be indirectly inferred when using model-based approaches [9], for example, by extrapolating measurement results to the nanoscopic case [10]. However, due to the averaging, these approaches cannot deliver a clear signature of dynamics below the length scale defined by the wavelength; instead they rely rather heavily on correct quantitative modeling of the system under study. Direct measurements at the length scale of interest, on the other hand, would deliver much more reliable and more model-independent results about nanoscopic details and concomitantly allow indirect methods to access even smaller length scales.

Therefore near-field optical techniques such as the probing on nanostructures or nanoholes [7, 11] have been used to downsize the measurement volume and to study processes at the nanoscale. However, these techniques are restricted to studies at or close to surfaces and their invasive nature may result in unwanted influence on the system under study. Therefore, these methods could not replace non-invasive far-field microscopy especially for dynamic studies on living cells. In an attempt to access smaller length scales, far-field microscopy was thus combined with single-particle tracking (SPT), using the much higher spatial localization accuracy of bright marker particles of down to below 10 nm [12, 13]. This however introduces other restrictions: to reach the desired spatial localization accuracy, SPT often applies bright but large and clumsy signal markers, which potentially influence the system under study. Further, the temporal resolution and statistical averaging of SPT still lacks far behind FCS and related techniques.

In the 1990s, the strategy of exploiting the spectral properties of the fluorescent markers themselves for overcoming the diffraction barrier paved the way to far-field nanoscopy [14]–[16]. A whole range of ‘diffraction-unlimited’ microscopy approaches has emerged since then [17], which despite their differences, are ultimately all based on switching the markers between a bright and a dark state to detect spatial features closer than the diffraction barrier sequentially in time. For example, sub-diffraction-resolution stimulated emission depletion (STED) nanoscopy [14, 18] uses stimulated emission to switch off fluorescence everywhere outside small, confined regions. These regions are then scanned across the diffraction limited volume to sequentially read out the spatial distribution of marker molecules within this volume. Far-field imaging with spatial resolutions down to the scale of ~ 20 nm has become routinely possible using this approach [19]. Because it allows continuous downscaling of the detection volume, STED seems ideally suited to adjust the measurement volume of fluctuation measurements to the length scale of interest and we have previously shown that it is indeed possible to observe single-molecule dynamics in nano-sized volumes in aqueous environment by combining STED with FCS [20]. However, this initial experimental realization also showed drawbacks. While the predicted decrease in focal volume could directly be measured from the dynamical single-molecule data, a concomitant relative

increase in unspecific background signal precluded accurate single-molecule measurements. Here, we explore the reason for this additional background in detail, determine conditions for an optimized nanoscopic single-molecule detection and extend our initial experiments accordingly. We show that the aforementioned unspecific background signal is caused by contributions of low fluorescence signal from axial out-of-focus volume shells in which the fluorescence ability of the dye was not entirely switched off by STED. In three-dimensional (3D) geometries, bias from these low-brightness contributions is minimized experimentally by decreasing the size of the confocal pinhole. Remaining contributions can be handled during analysis by a global FCS–FIDA approach and we thus demonstrate the study of freely diffusing dye molecules in an open measurement volume, confined more than 25-fold compared to the confocal case. Our approach is feasible for both 2D and 3D focal confinement, and with both pulsed and continuous-wave (CW) irradiation.

Importantly, unspecific out-of-focus background is absent when measuring on 2D samples. Consequently, STED nanoscopy studies of single-molecule dynamics on membranes feature excellent signal-to-noise ratios, thereby allowing continuous down-scaling of the focal spot, in the present experiments down to 30 nm in diameter. Here, we demonstrate nanoscale observation of the heterogeneous diffusion behavior of fluorescent phosphoglycero- and sphingolipids in the plasma membrane of living cells and determine on/off rates of their nanoscale trapping to other membrane constituents. While phosphoglycerolipids almost diffuse freely, trapping is pronounced for the sphingolipids with on and off rates of $\sim 80 \text{ s}^{-1}$. Consequently, the combination of fluctuation analysis with STED-engineered ultra-small measurement volumes sheds new light on prominent biological problems such as the putative formation of ‘lipid rafts’, which are assumed to play an important functional role in cells.

2. Experimental

2.1. Dye solution

The organic dye Atto647N (fluorescence excitation and emission maxima of 645 and 670 nm, respectively; Atto-Tec, Siegen, Germany) was dissolved either in PBS buffer (pH 7.5) or 2,2'-thiodiethanol (TDE, Sigma-Aldrich; 96%, 4% water) to a final concentration of 1–10 nM. We performed measurements of the free diffusing dyes at 22 °C in 100 μl samples sealed on microscope cover glass.

2.2. Multilamellar layer

We put 100 μl of phospholipid blend (DOPE (1,2-dioleoyl-*sn*-glycero-3-phosphoethanolamine), DOPS (1,2-dioleoyl-*sn*-glycero-3-phosphoserine), DOPC (1,2-dioleoyl-*sn*-glycero-3-phosphocholine) (Avanti polar lipids, Alabaster, AL) 5 : 3 : 2 in chloroform 10 mg ml⁻¹, stored at -20 °C under N₂-atmosphere) on a cover slip and subsequently evaporated it under vacuum for roughly 1.30 h. Afterwards the dried lipids were swelled in distilled water to a multilamellar layer for half an hour and rinsed two or three times. For fluorescence measurements, 1 μl of a 0.01 mg ml⁻¹ solution of an Atto647N labeled phosphoglycerolipid (Atto647N-1,2-dipalmitoyl-*sn*-glycero-3-phosphoethanolamine, Atto-Tec, referred to as Atto647N-PE) was added to the phospholipid blend before evaporation to yield a dye/lipid molar ratio of approximately 1 : 100 000.

2.3. Horizontal black lipid bilayer

To perform measurements on a horizontal lipid bilayer (black lipid bilayer), L- α -phosphatidylcholine lipid (type S-IV, Sigma-Aldrich, Steinheim, Germany) was kept at -20°C in a chloroform/methanol (1 : 1) mixture at 50 mg ml^{-1} . After vacuum evaporation of $100\ \mu\text{l}$ of the stock solution we solved the lipid in $100\ \mu\text{l}$ n-decane. Planar lipid bilayers were created using a modified painting technique in a setup depicted in figure 6(d) [21, 22]. Briefly, a drop of lipid was smeared over a small hole of $\sim 100\ \mu\text{m}$ in diameter in a Teflon foil separating two water-filled chambers. The lower chamber was bordered by a microscope cover glass, resulting in a cover glass-to-bilayer distance of approximately $100\text{--}150\ \mu\text{m}$. After the evaporation of n-decan, a stable lipid bilayer forms spontaneously. To perform FCS measurements on the bilayer membranes, we added $10\ \mu\text{l}$ of the 0.01 mg ml^{-1} solution of the Atto647N labeled phosphoglycerolipid Atto647N-PE (see above) to the S-IV-lipid before evaporation to yield a dye/lipid molar ratio of $\sim 1 : 50\ 000$.

2.4. Cellular membrane

We incorporated fluorescent lipid analogues into the plasma membrane of living PtK2 cells. The cells were seeded on no.1 thickness standard glass coverslips (diameter 25 mm) to a confluence of about 80%. The cells were grown at 37°C in a water-saturated atmosphere of 5% CO_2 in air. All media and supplements were purchased from Invitrogen. We used the following fluorescent lipids in our live-cell measurements: the phosphoglycerolipid Atto647N-PE (see above) and the sphingolipid *N*-(Atto647N)-sphingosylphosphocholine (*N*-Atto647-sphingomyelin, Atto-Tec, referred to as Atto647N-SM). Complexes of the labeled lipids and bovine serum albumin (BSA) were prepared according to Martin and Pagano [23] and Schwarzmann *et al* [24] with slight modifications. Briefly, $100\ \text{nmol}$ of the lipid stock solutions ($\text{CHCl}_3/\text{MeOH}$, 3 : 1) were dried under a stream of nitrogen. The dried lipids were dissolved in $20\ \mu\text{l}$ of absolute ethanol and vortexed vigorously after addition of 1 ml of defatted BSA solution ($100\ \mu\text{M}$, i.e. $10^{-4}\ \text{M}$ defatted BSA in Dulbecco's Modified Eagle Medium (DMEM) without phenol-red buffered with 10 mM HEPES). Addition of 9 ml HDMEM (HEPES + DMEM = HDMEM) resulted in a final concentration of $10\ \mu\text{M}$ BSA and 0.2% ethanol. In the case of PE, the BSA concentration was twice as large ($2 \times 10^{-4}\ \text{M}$). Afterwards, cells were washed with HDMEM and incubated with BSA-lipid-complexes ($5\text{--}50\ \text{nM}$ in the case of Atto647N-SM and $10\text{--}300\ \text{nM}$ in the case of Atto647N-PE) on ice for 30 min, washed in cold HDMEM and incubated at 37°C for 4 min in HDMEM. Measurements were performed at room temperature ($22\text{--}24^{\circ}\text{C}$). We excluded diffusion of non-integrated fluorescent lipids by control measurements in between the cells.

2.5. STED microscope

We incorporated a standard epi-illuminated confocal microscope for our fluorescence experiments. Fluorescence excitation was performed with a 633 nm pulsed laser diode ($\sim 80\ \text{ps}$ pulse width, LDH-P-635, Picoquant, Berlin, Germany) or a CW laser diode (FiberTEC635; AMS Technologies, Munich, Germany). We supplied the STED light by a Titan:Sapphire laser system (MaiTai, Spectra-Physics, Mountain View, CA; or Mira 900F, Coherent) running at $750\text{--}780\ \text{nm}$ and with a repetition rate of 76 and 80 MHz, respectively, or the Mira 900F system operated in CW at 780 nm. In the case of pulsed irradiation, the repetition

rate of the STED laser was taken as trigger for the excitation laser with timing adjustment between the excitation and STED pulse performed by a home-build delay electronic. At optimum, the STED pulse immediately followed and partially overlapped with the excitation pulse. We controlled and stabilized the STED power by a laser power controller unit (LPC, Brockton Electronics, Brockton, MA) and coupled the linearly polarized STED beam through a 120 m long polarization-maintaining single-mode fiber (AMS Technologies) for stretching the pulses to about 250–300 ps. After spatial overlay of both laser beams with appropriate dichroic filters (AHF Analysentechnik, Tübingen, Germany) they were directed on a beam-scanning device (mirror tilting system PSH 10/2, Piezosystem Jena, Jena, Germany) and into the microscope (DMIRBE, Leica Microsystems, Mannheim, Germany). We applied an oil immersion objective (PLAPON 60 \times NA = 1.42, Olympus, Japan, or HCXPLAPO NA = 1.4, Leica) to focus the laser light to a diffraction-limited spot on the sample and to collect the fluorescence emission. In the case of the horizontal lipid bilayers, we used a water immersion objective (UPLSAPO 60 \times NA = 1.2, Olympus). The axial position of the focal spots was adjusted by an objective lens positioning system (MIPOS 250, Piezosystem Jena). We produced a doughnut-shaped focal spot with a central zero of the STED light by introducing a phase plate into the beam path, imprinting a helical phase ramp $\exp(i\varphi)$ with $0 \leq \varphi \leq 2\pi$ on the wave front and introducing a $\lambda/4$ plate for circular polarization of the beam in front of the objective. For axial confinement, we introduced a phase plate into the linear polarized STED light beam that π -phase shifted the central half of the wave front incident on the objective (the beam was again circularly polarized by a $\lambda/4$ plate in front of the objective). In the case of both lateral and axial phase confinement, the linearly polarized STED beam was split up by a polarizing beam splitter, each divided beam traversed one of the two different phase plates, and both beams were again re-combined by another polarizing beam splitter before being circularly polarized by a $\lambda/4$ plate in front of the objective. The respective powers of STED light for the lateral and axial confinement were controlled by a $\lambda/2$ plate in front of the first polarizing beam splitter. In our 3D confinement experiments the power of the STED light was evenly split up onto both beam paths. The fluorescence was imaged back over the beam-scanning device and coupled into a multi-mode 50 : 50 fiber splitter (Fiber Optic Network Technology, Surrey, Canada) with an aperture size corresponding to $1.4\times$ the magnified confocal fluorescence spot (if not otherwise specified). The fluorescence signals were then detected by two single-photon counting units (avalanche photo diode SPCM-AQR-13-FC, Perkin Elmer Optoelectronics, Fremont, CA). We blocked potential contributions from scattered laser light or unwanted autofluorescence by appropriate fluorescence filtering (AHF). The fluorescence counts were further processed by a hardware correlator (Flex02-01D, Correlator.com, NJ) for FCS and FIDA. We calculated the excitation intensity I_{exc} from the power P_{exc} incident on the sample and the focal area A_{exc} ; $I_{\text{exc}} = P_{\text{exc}}/A_{\text{exc}}$. We determined $A_{\text{exc}} \approx \pi(\text{FWHM}_{\text{exc}}/2)^2$ from the diameter FWHM_{exc} (full-width at half-maximum) of the conventional diffraction-limited focal spot. The values of $\text{FWHM}_{\text{exc}} \approx 240$ nm for the oil immersion and ≈ 330 nm for the water immersion objective were measured by scanning over a scattering gold bead of sub-diffraction diameter (80 nm gold colloid, En.GC80, BBInternational, Cardiff, UK) and detecting the scattered signal on a non-confocal detector (MP 963 Photon Counting Module, Perkin Elmer). The intensity of the excitation light was usually 25 kW cm^{-2} . For the STED light, we indicate the power P_{STED} incident on the sample. The maximum pulse peak intensity of the focal spot of the STED light can be estimated by $I_{\text{STED,P(max)}} \approx k P_{\text{STED}}/A_{\text{STED}}/(\tau_P f)$ with a scaling factor $k = 1$ for the non-engineered spot and $k = 0.3$ and 0.5 for the spots engineered for lateral

and axial confinement, respectively, the pulse duration τ_p , and the pulse repetition rate f . $A_{\text{STED}} \approx \pi(\text{FWHM}_{\text{STED}}/2)^2$ denotes the focal area of the non-engineered spot of the STED light and was determined by the experimentally measured focal diameter $\text{FWHM}_{\text{STED}} \approx 340$ nm (oil immersion objective) or 400 nm (water immersion objective). For calibration of the STED microscope with lateral confinement, we determined the diameters of the effective fluorescence foci by scanning approximately 20 nm large fluorescent crimson beads (Molecular Probes, Eugene, OR) for the various STED powers and established the radii (at half-maximum of the detected signal intensity) of the accordingly imaged beads.

2.6. FCS

FCS [1]–[3] analyses the temporal fluctuations $\delta F(t) = F(t) - \langle F(t) \rangle$ of the detected fluorescence signal $F(t)$ by calculating the normalized second-order auto-correlation function $G_N(t_c)$,

$$G_N(t_c) = 1 + \langle \delta F(t) \delta F(t + t_c) \rangle / \langle F(t) \rangle^2, \quad (1)$$

with correlation time t_c and angular brackets indicating averaging over the measurement time t . Fluctuations $\delta F(t)$ may stem from single dye molecules diffusing in and out of the detection volume or transiently turning dark due to, for example, transition into their metastable dark triplet state. We analyzed the correlation data according to common FCS theory [25].

$$G_N(t_c) = 1 + G_N(0)[G_D(t_c)G_T(t_c)], \quad (2a)$$

with

$$G_D(t_c) = (1 + t_c/\tau_{xy})^{-1}(1 + t_c/\tau_z)^{-1/2}, \quad (2b)$$

$$G_T(t_c) = 1 + T/(1 - T) \exp(-t_c/\tau_T), \quad (2c)$$

describing diffusion and triplet state dynamics. Here, a spatial 3D Gaussian profile of the detected fluorescence was assumed. The lateral $\tau_{xy} = r_{xy}^2/(2D \ln 2)$ and axial transit time $\tau_z = r_z^2/(2D \ln 2)$ through the 3D Gaussian profile are given by the diffusion constant D and the lateral and axial radii r_{xy} and r_z of the 3D Gaussian profile, respectively. The radii are defined at half the maximum of the Gaussian intensity distribution and r_{xy} complies with the focal radius defined in equation (19). Further, on–off blinking of the molecular fluorescence from the transition into the dye’s dark triplet state was regarded in the FCS analysis by the characteristic parameters of an average triplet population T and a triplet correlation time τ_T [25].

With the general 3D spatial coordinate r , the spatial profile of the detected fluorescence $Q(r) = Q_0 h(r)$ is expressed by the product of the maximum focal brightness Q_0 , i.e. maximum instantaneous count-rate per single fluorescing molecule, and the spatial fluorescence detection profile $h(r)$ with $h(0) = 1$. $h(r)$ is defined through the focal intensity distribution of the excitation laser, the resulting spatial profile of fluorescence emission (including spatial dependent saturation of fluorescence excitation) and the spatial detection efficiency. The latter results from the point-spread function of the imaging system and the diameter of the confocal pinhole. $h(r)$ slightly deviates from a 3D Gaussian distribution. However, the inclusion of more complex spatial profiles would result in a drastic increase of complexity of FCS analysis with only little effect on the resulting data. Because the Gaussian approximation fitted all of our correlation data well, we used it throughout the manuscript; we can safely assume that the

decay of the correlation curves, i.e. the values of τ_{xy} and τ_z give a good estimate of the relative confinement of the measurement volume by STED.

The amplitude $G_N(0)$ of the correlation curve is inversely proportional to the average number of dye molecules in the detection volume. For negligible background signal, one usually defines a number of molecules N_{fcs} by

$$G_N(0) = 1/N_{fcs}, \quad (3)$$

where $N_{fcs} = cV_{fcs}$ with c being the physical concentration in molecules per unit volume. The volume V_{fcs} is defined by the size and form of the detection volume,

$$V_{fcs} = V^2 / \int h(r)^2 dr^3 = V/\gamma, \quad (4)$$

where the actual detection volume V is given by the volume integral

$$V = \int h(r) dr^3 \quad (5)$$

and the factor $\gamma = V/V_{fcs}$ parameterizes the deviation of its shape from a box. The definition of V_{fcs} and consequently N_{fcs} results from the normalization of the correlation function by $\langle F(t) \rangle^2$ (equation (1)). V_{fcs} and N_{fcs} are determined by all contributions of the detection volume, i.e. also molecules of low fluorescence brightness in the focal periphery contribute significantly to N_{fcs} .

2.7. FIDA

While FCS analyzes the temporal characteristics of the fluctuating fluorescence signal, FIDA (or PCH) [4, 5] extracts information from the amplitudes of the fluctuating fluorescence signal $F(t)$. Specifically, a frequency histogram $P(n)$ is formed from the number of counts n recorded in successive time intervals of fixed duration ΔT . Fitting of a theoretical distribution to $P(n)$ provides a specific fluorescence brightness q , i.e. a detected count-rate per single molecule, a particle number N of the fluorescent molecule under study, and the amount of background signal B_b .

For a theoretical description of $P(n)$, FIDA has to account for the inhomogeneous spatial fluorescence detection profile $h(r)$. While the actual shape of $h(r)$ is of no importance, an accurate description of $P(n)$ requires the knowledge of the relative volume size that a specific fluorescence brightness spans. In FIDA, the units of brightness are often chosen differently than in FCS and the apparent brightness profile $B(r) = B_0 h(r)$ is introduced alongside a new, dimensionless variable $w = \ln(B_0/B(r)) = -\ln(h(r))$. The volume element ΔV_i defined by a small brightness interval Δw around the brightness w_i is described with sufficient accuracy by a function with three additional fitting parameters a_0 , a_1 and a_2 [26].

$$\Delta V_i = V'(w) \Delta w = A_0 w_i^{a_2} [1 + a_0 w_i + a_1 w_i^2] \Delta w \quad (6)$$

where the derivative $V'(w) = dV/dw$ describes the differential weight of regions with brightness w and the choice of the parameter A_0 defines the units of concentration. The system parameters a_0 , a_1 and a_2 are empirical and can be determined by calibrating the optical system with a standard dye sample. The number of counts detected from the volume fraction ΔV_i is characterized by fluctuations in the average particle number and in the number of photon counts n detected per time window ΔT , both given by Poisson distributions. Thus, for a dye

of concentration C and brightness q the probability $P_i(n)$ to detect n photons from the section ΔV_i of the detection volume is given by

$$P_i(n) = \sum_{m=0}^{\infty} \left[\frac{(C \Delta V_i)^m}{m!} \exp(-C \Delta V_i) \right] \left[\frac{(mq B(w_i) \Delta T)^n}{n!} \exp(-mq B(w_i) \Delta T) \right]. \quad (7)$$

Here, $q B(w_i) = q B_0 \exp(-w_i)$ denotes the brightness (i.e. the expectation value of the detection rate of fluorescence photons per molecule) of a dye located in ΔV_i and m is the number of fluorescing molecules present in the volume fraction. The overall theoretical photon count probability function $P(n)$ is then given by the convolution over all volume contributions $P_i(n)$ and the Poisson photon count distribution $P_b(n)$ accounting for a possible background photon rate B_b

$$P_b(n) = (B_b \Delta T)^n / n! \exp(-B_b \Delta T). \quad (8)$$

In FIDA, convolution is performed efficiently through the principle of generating functions replacing the convolution of the $P_i(n)$ by the multiplication of their generating functions [5, 26]. For $\Delta w \rightarrow 0$, the generating function of $P(n)$ can eventually be written as a 1D integral over w which is then fitted to the experimental distributions to obtain estimates for C and q . As mentioned above, their units are determined by the choice of constants B_0 and A_0 . It is conventional to fix them such that, in the units of volume defined by A_0 , the integrals $\int B \, dV = \int B(w) V'(w) \, dw$ and $\int B^2 \, dV$ are normalized to unity [5]. In this case $B_0 = 1/\gamma = V_{\text{fcs}}/V$ and the concentration and brightness fit parameters are scaled such that $C = N_{\text{fcs}} = c V_{\text{fcs}}$ and $q = Q_0/B_0 = \gamma Q_0$ with the particle number N_{fcs} and the fluorescence detection volume V_{fcs} defined in equations (3) and (4), the focal peak brightness Q_0 and the factor γ given by equation (4). Again, the values N_{fcs} and q average over all detection volume contributions, even over low-brightness contributions of, for example, the focal periphery. The historical reason for this convention is that, if scaled in this way, $C = N_{\text{fcs}}$ and q can be calculated directly from moment analysis [27] if the background contribution is negligible.

2.8. Apparent particle number and brightness

In FCS, the main contribution to the initial drop of the correlation curve from which the transit time is determined comes from molecules during their passage of volume shells with large fluorescence brightness. This results naturally from the square dependence of the correlation curve on the fluorescence signal (equation (1)). On the other hand, especially in cases of spatial profiles $h(r)$ with large volume contributions of low fluorescence brightness, the particle number N_{fcs} and the brightness q directly resulting from FCS and FIDA reflect averages over the total detection volume and do not describe those molecules well that effectively contribute to the fluctuation data. In fact, the actual number of molecules $N = cV$ in the detection volume V (equation (5)) and the peak focal brightness Q_0 would be a much more intuitive measure, because they properly weigh the behavior of molecules in the focal center, i.e. in volume parts of high fluorescence brightness more strongly. For any given form $h(r)$ of the detection volume, a proper determination of the brightness as well as the particle number N and thus concentration from the correlation function's amplitude would require the calculation of the scaling factor γ using equation (4)

$$G_N(0) = \gamma/N. \quad (9)$$

Again, this direct relation is valid only for negligible background. Calculation of γ requires exact knowledge of the detection volume's shape $h(r)$. However, when reducing the detection volume by STED, exact determination of $h(r)$ especially in the areas of low brightness is difficult and calculating N using equation (9) is thus inaccurate. We therefore make a heuristic approach to determine realistic values of the particle number N and the molecular brightness Q_0 without exact knowledge of $h(r)$. We approximate the form of a fluorescence detection profile $h(r)$ with large volume contributions of low brightness (and thus a low, unknown value of γ) by the form of a compact profile $h^*(r)$ with a larger scaling factor $\gamma^* > \gamma$ (which is, for example, described by the brightness–volume relation of a standard confocal microscope) and a pseudo background signal B_{pseudo} that takes into account contributions from the neglected low-brightness volume shells. In FIDA, this can be realized by fixing the system parameters a_0 , a_1 and a_2 to the values determined by confocal calibration measurements. One then obtains an apparent particle number N^* , an apparent brightness q^* and an apparent background or low-brightness signal B_b^* when fitting the histogram data $P(n)$. In this way, FIDA splits up the overall average signal count-rate $\langle F(t) \rangle$ into dedicated large and low brightness signal contributions

$$\langle F(t) \rangle = N^* q^* + B_b^*. \quad (10)$$

Here, FIDA fits will estimate only the total (apparent) background signal $B_b^* = B_b + B_{\text{pseudo}}$, where B_b stands for possible ‘normal’ background signal such as scattered laser light. Importantly, since γ^* is now independent of the amount of volume reduction achieved by STED, both N^* and q^* are not influenced by contributions of the resulting low-brightness signal from outer shells which is now completely covered by B_{pseudo} . Thus, changes in N^* ($\sim V$) now reveal the true confinement and q^* ($\sim Q_0$) reflects the true reduction of the focal peak brightness.

Once B_b^* is known, we can use the same approach in FCS. By relating the apparent background signal B_b^* as previously determined by FIDA to the total signal count-rate $\langle F(t) \rangle$, the apparent particle number N^* can be calculated from the amplitude $G_N(0)$ [28]:

$$G_N(0) = (1 - B_b^*/\langle F \rangle)^2 / N^*. \quad (11)$$

With this, the relative decrease of the factor γ with focal confinement by STED can well be estimated by the ratio N^*/N_{fcs} .

2.9. FIDA correction

For very small sampling intervals and sufficient photon statistics, the values of particle numbers determined by FIDA are equal to those determined by FCS. For finite sampling intervals, $\Delta T > 0$ ($50 \mu\text{s}$ in our experiments), however, deviations may occur. For example, if $\Delta T > \tau_{xy}$ one would average over a whole molecular transit, effectively smearing out the volume shells. As a consequence, FIDA would obtain lowered brightness values $q(\Delta T)$ and increased particle numbers $N(\Delta T)$ [29]. This bias can be corrected for. Because the following relations hold for both the primary parameters N_{fcs} and q and the apparent values N^* and q^* , we will keep to a general notation N and q . To a good approximation, both the particle number and the brightness scale with the same correction factor $S < 1$:

$$N = N(\Delta T)S, \quad (12a)$$

$$q = q(\Delta T)/S, \quad (12b)$$

where S is a function of the ratio $\tau_{xy}/\Delta T$:

$$S = [1 + \Delta T/(6a)(2/\tau_{xy} + 1/\tau_z)]^{-a} \approx [1 + (3a/(\tau_{xy}/\Delta T))^{-1}]^{-a}. \quad (12c)$$

The transit time τ_{xy} can be determined, e.g. from complementing FCS analysis [29]. Neglecting the axial transit time τ_z is valid since τ_z is usually much larger than the lateral transit time τ_{xy} . Common values of the empirical factor a are $< 2/3$ [29] and consequently, S significantly deviates from 1 only if $\tau_{xy}/\Delta T < 1$. Therefore, with $\Delta T = 50 \mu\text{s}$ in our experiments, we expect significant corrections only in the case of aqueous environment ($\tau_{xy} = 8\text{--}80 \mu\text{s}$), while τ_{xy} exceeds $50 \mu\text{s}$ in the TDE or membrane measurements, even for strong focal confinement by STED. The use of smaller time windows $\Delta T < 50 \mu\text{s}$ is possible, but results in small numbers of photon counts n , reducing the number of data points of $P(n)$ and making FIDA fitting impractical. We corrected the FIDA parameters determined from the aqueous environment measurements using $a = 0.15$, which has been estimated from the global FCS–FIDA analysis as outlined in the appendix. Remaining differences between the values of N and q determined by FIDA and FCS may be explained by a slightly incorrect value of a as well as the fact that we (to make simultaneous recording of histogram and correlation data possible) have used a cross-correlation between the signal detected on our two detectors for FCS but gained the histogram data for FIDA only from one single detector.

2.10. FCS analysis of lipid membrane diffusion

Diffusion along the axial z -direction is absent in 2D samples such as membranes, dropping the axial diffusion term τ_z in equation (2)

$$G_D(t_c) = (1 + (t_c/\tau_{xy})^\alpha)^{-1}. \quad (13)$$

The anomaly $(1/\alpha)$ accounts for hindered diffusion, which is commonly encountered in live cell measurements [9]. While $(1/\alpha) = 1$ corresponds to a free Brownian diffusion with a constant diffusion coefficient D , $(1/\alpha) > 1$ characterizes anomalous subdiffusion with an apparently lower diffusion coefficient for large-scale motion. As before, the radial transit time is defined as $\tau_{xy} = r_{xy}^2/(2D \ln 2)$ with D and r_{xy} being the (apparent or averaged) diffusion constant (including subdiffusion) and lateral radius, respectively. Subdiffusion may, for example, be caused by transient trapping due to binding of the diffusing molecule to a fixed or comparatively slow moving particle. Such reactions are described by the on/off kinetic of the binding process to an immobile complex in the diffusion path of the molecule with an effective encounter rate constant k_{on} (denoted on-rate throughout) and off rate k_{off} . If the trapping time $1/k_{\text{off}}$ is much longer than the average time the freely diffusing molecule would spend in the observation focus, the diffusion is reaction dominated and we can describe the correlation function by

$$G_D(t_c) = (1 - B)(1 + (t_c/\tau_{\text{free}}))^{-1} + B \exp(-k_{\text{off}}t_c), \quad (14)$$

where $\tau_{\text{free}} = r_{xy}^2/(2D_{\text{free}} \ln 2)$ is the average focal transit time for free diffusion (with free diffusion constant D_{free} not including subdiffusion) and the fraction $B = 1/(1 + k_{\text{on}}/k_{\text{off}})$ quantifies the influence of trapping on diffusion [30]. In case, diffusion is not dominated by trapping, we may follow the derivation laid out by Michelman-Ribeiro *et al* [30],

$$G_D(t_c) = \frac{r_{xy}^2}{8\pi} \int \int \Gamma(q) \Omega(q, t_c) d\vec{q}, \quad (15)$$

where $\vec{q} = (q_x, q_y)$ is the Fourier transform variable, $\Gamma(q) = \exp(-q^2 r_{xy}^2/4)$ accounts for the assumed Gaussian brightness profile and the term

$$\Omega(q) = (1 + \phi) \exp[(\alpha + \beta)t_c] + (1 - \phi) \exp[(\alpha - \beta)t_c] \quad (16)$$

comprises diffusion and chemical kinetics with

$$\phi = [k_{\text{on}} + k_{\text{off}} + q^2 D_{\text{free}}(k_{\text{on}} - k_{\text{off}})/(k_{\text{on}} + k_{\text{off}})]/2\beta, \quad (17)$$

where $\beta = \sqrt{\alpha^2 - q^2 D_{\text{free}} k_{\text{off}}}$ and $\alpha = -(q^2 D_{\text{free}} + k_{\text{on}} + k_{\text{off}})/2$ and D_{free} is the diffusion coefficient of free diffusion. In our fits we used k_{on} and k_{off} as free parameters and usually fixed $D_{\text{free}} = 5 \times 10^{-9} \text{ cm}^2 \text{ s}^{-1}$ to the value estimated from the confocal data and known from previous results [31]. As outlined in the text, fitting with values of $D_{\text{free}} = 4\text{--}6 \times 10^{-9} \text{ cm}^2 \text{ s}^{-1}$ yields similar results.

2.11. Monte Carlo simulation of lipid membrane diffusion

We used Monte Carlo simulations to check the validity of the trapping model for the observed correlation data. The simulations generated fluorescence time traces of the planar diffusion pathways of the fluorescent lipids through a Gaussian focal spot area of varying diameter (full width at half maximum = 20–225 nm), undergoing transient binding to fixed particles with on and off rates k_{on} and k_{off} . The lipids were assumed to diffuse freely between binding with a diffusion coefficient of $D_{\text{free}} = 5 \times 10^{-9} \text{ cm}^2 \text{ s}^{-1}$ which agrees with that from our experimental findings. Initially, 100 lipid molecules were distributed randomly on a simulation support area of $1 \mu\text{m} \times 1 \mu\text{m}$. The simulations featured stochastically stable results after 5×10^6 time steps of $1 \mu\text{s}$ length using a focal maximum brightness of 1000 MHz. The symmetrically normalized auto-correlation curves of the fluorescence time traces were numerically calculated using the multi-tau correlation method [32]. Fitting equation (13) to the simulated correlation data reveals values of average transit time τ_{xy} that are compared to the experimental values τ_{xy} for the different focal diameters.

3. Results and discussion

3.1. Principle of STED nanoscopy

The basic concept of STED nanoscopy is shown in figure 1. Excitation of a fluorescence marker is superimposed by red-shifted (STED) laser light. Inducing stimulated emission, an increasing power P_{STED} of this STED light efficiently switches off the detected fluorescence, driving this excited state prohibition far into saturation (figure 1(a)). Combining the conventional diffraction-limited excitation spot with an engineered focus of the STED light featuring an irradiation spot with a sharp local intensity zero, large P_{STED} switch off fluorescence everywhere but at the local intensity zero. This arrangement leaves an effective fluorescence spot of dimensions far below the diffraction limit (figure 1(b)). Importantly, varying the power of the light driving the switching process allows tuning of the lateral radius r_{xy} of the effective fluorescence spot, which can be estimated by a modification of Abbe's equation [6, 33, 34],

$$r_{xy} \approx 0.6 \frac{\lambda}{2\text{NA} \sqrt{1 + P_{\text{STED}}/P_{\text{SAT}}}}, \quad (19)$$

with the wavelength λ of the fluorescence light, the numerical aperture (NA) of the microscope objective, the incident STED power P_{STED} and the saturation power P_{SAT} being a characteristic

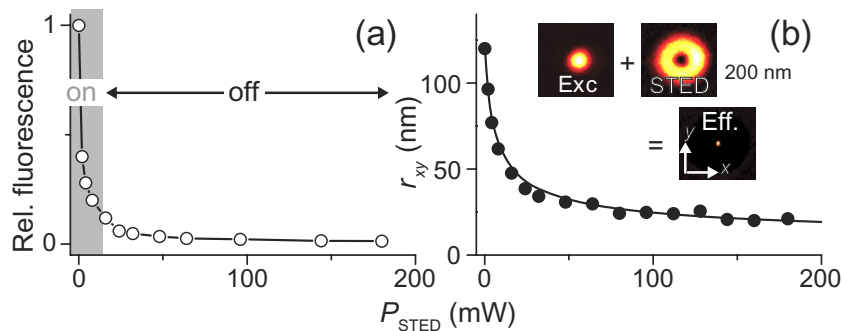


Figure 1. Far-field optical STED nanoscopy. (a) STED nanoscopy is based on switching off the fluorescence ability of a dye by a beam of light inducing stimulated emission. Increasing the power P_{STED} of the STED beam increases the probability of fluorescence state inhibition. (b) The effective focal fluorescence spot is of sub-diffraction size (Eff. Inset), created by a focal intensity distribution of the STED light with a local zero (STED inset) that is overlaid with the diffraction-limited excitation spot (Exc inset). The lateral radius r_{xy} of the effective focal fluorescence spot decreases with the power P_{STED} of the STED light (experimental data (circles) and fit of equation (19) to the data with $P_{\text{SAT}} = 3$ mW (line)). The data depicted were recorded on ~ 20 nm sized crimson fluorescent beads: relative (Rel.) fluorescence state inhibition when combining the excitation spot with a non-engineered, diffraction-limited focal STED spot (a), and average lateral radius r_{xy} determined from the STED images with doughnut-shaped focal STED spot (b). The lateral xy intensity distributions of the excitation and STED light (inset (b)) were both measured by scanning a scattering sub-diffraction-sized gold bead through the focal region. The effective lateral fluorescence spot of the STED microscope (inset (b)) was measured on a fluorescence crimson bead with $P_{\text{STED}} = 150$ mW.

of the fluorophore in use given a certain spatial distribution of the STED light [34]. Consequently, by increasing P_{STED} the spatial resolution of a STED microscope can be dynamically optimized, potentially to a maximum possible, i.e. to molecular scales.

3.2. Aqueous environment

Figure 2(a) shows fluorescence correlation (FCS) data $G_N(t_c)$ (equation (1)) recorded for the organic dye Atto647N in aqueous PBS buffer with and without addition of focal-engineered STED light. In a first place, the correlation curve encodes the average molecular transit time through the focal detection volume, which follows from the decay of the correlation data, and the average number N_{fcs} of fluorescing particles in the detection volume, which is inversely proportional to the correlation function's amplitude $G_N(0) = 1/N_{\text{fcs}}$ (equation (3)). A reduction of the detection volume by STED should result in a decrease of both the transit time and N_{fcs} , which in turn should allow revealing nanoscale details of molecular dynamics and performing FCS at larger concentration, respectively. According to the decrease of transit time and N_{fcs} , the decay of $G_N(t_c)$ should shift to shorter correlation times t_c and $G_N(0)$ should increase. While our experimental FCS data outlines the expected shift of the correlation curve to lower t_c , we observed an unexpected decrease in amplitude $G_N(0)$ with P_{STED} .

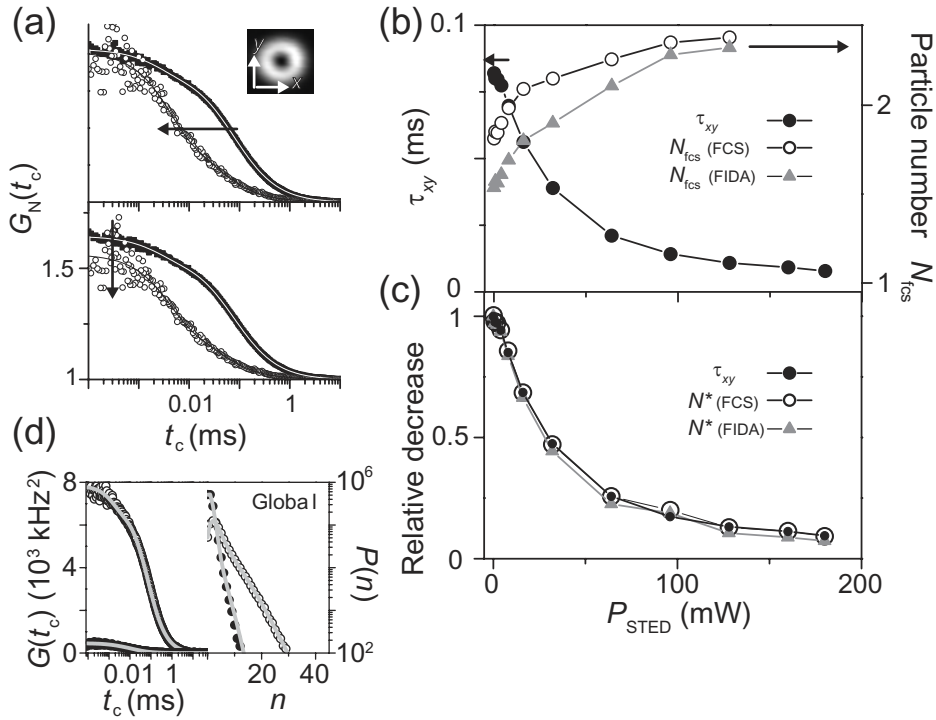


Figure 2. STED-FCS/FIDA of the dye Atto647N in aqueous solution. (a) Correlation data $G_N(t_c)$ at confocal (black circles) and STED recording (open circles) with $P_{\text{STED}} = 50$ mW (780 nm) and the doughnut-shaped intensity distribution of the STED light (inset) together with fits (grey lines) of equation (2) to the data: normalization at $t_c = 0.001$ ms (upper panel) and original data (lower panel), showing a decrease of the decay time and amplitude upon focal confinement (arrows). (b) Dependence of transit time τ_{xy} (black circles) and particle numbers N_{fcs} determined by FCS (open circles) and FIDA (grey triangles) on the STED power P_{STED} . (c) Relative dependence of transit time τ_{xy} (black circles) and apparent particle numbers N^* determined by FIDA (grey triangles) or FCS (open circles) on the STED power P_{STED} . (d) Global FCS-FIDA analysis. Un-normalized correlation $G(t_c)$ (left panel) and histogram data $P(n)$ (right panel) for confocal (open circles) and STED recording (closed circles, $P_{\text{STED}} = 160$ mW) together with the global FCS-FIDA fit (grey lines) to the experimental data.

To this end, we recorded FCS data with increasing power P_{STED} of STED light at a constant excitation intensity of 25 kW cm^{-2} , and fitted equation (2) to the data. The STED light featured a doughnut-like intensity distribution with a central zero along the lateral x/y -directions (inset figure 2(a)). Increasing the power P_{STED} of the STED light consequently reduced the focal volume along the lateral directions only, leaving the axial extension unchanged. As a result, the values of τ_{xy} decreased and those of τ_z remained unchanged. Apart from negligible light-induced triplet depopulation [35], the STED light does not alter the triplet population. We determined $\tau_z = 4$ ms, $T = 0.14$ and $\tau_T = 3 \mu\text{s}$ from confocal FCS data and fixed these values throughout further analysis. Figure 2(b) depicts the dependence of the resulting values of

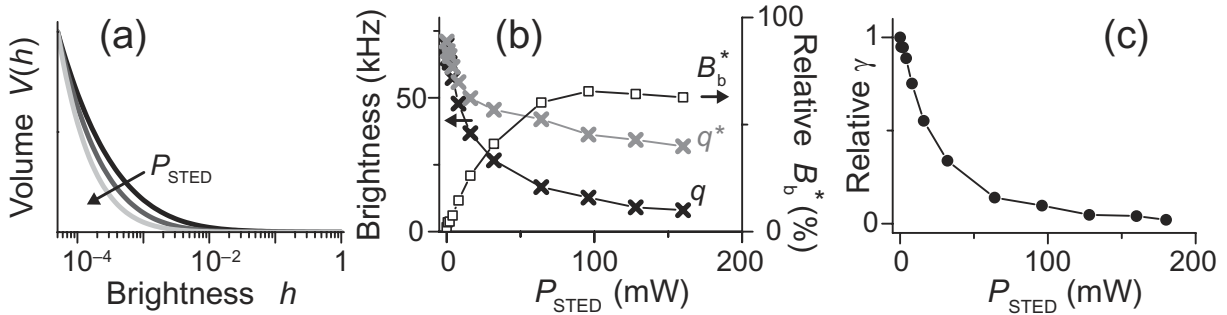


Figure 3. STED–FIDA of the dye Atto647N in aqueous solution. (a) Relative volume size $V(h)$, a relative brightness h spans for $P_{\text{STED}} = 0$ mW (black line), 64 mW (grey line) and 160 mW (light grey line), depicting a relative increase of volume fractions with low brightness (arrow). (b) Dependence of the fluorescence brightness q , of the apparent fluorescence brightness q^* and of the relative fraction of apparent low-brightness background B_b^* of the total detected signal on the STED power P_{STED} . (c) Relative dependence of the scaling factor γ of FCS analysis on P_{STED} calculated using the ratio N^*/N_{fcs} .

τ_{xy} and N_{fcs} on P_{STED} . While τ_{xy} decreases with P_{STED} from $80 \mu\text{s}$ at confocal recordings ($P_{\text{STED}} = 0$ mW) down to $8 \mu\text{s}$ at $P_{\text{STED}} = 180$ mW by a factor of ~ 10 , N_{fcs} increases from 1.8 up to 3.3 by a factor of 1.3. The 10-fold decrease of τ_{xy} outlines a congruent confinement of the focal area and a $\sqrt{10} \approx 3.3$ -fold reduction of the focal spot diameter. The particle number $N_{\text{fcs}} = cV_{\text{fcs}}$ scales with the dye concentration c and the detection volume V_{fcs} defined in FCS (equation (4)). Since c stays constant, the observed increase of N_{fcs} depicts an enlargement of V_{fcs} , which is contrary to the volume decrease rendered by τ_{xy} . While equation (2) fits our FCS data well, N_{fcs} and V_{fcs} seem to be an inaccurate measure of our experimental conditions.

We used FIDA [4, 5] to complement our FCS data. We acquired the PCH data $P(n)$ along with the FCS data and used FIDA to fit $P(n)$ resulting in values of the particle number N_{fcs} , the fluorescence brightness q and the system parameters a_0 , a_1 and a_2 . We fixed the background count-rate B_b to 1 kHz as measured for scattering signal on a pure PBS solution. Similarly to the FCS analysis, N_{fcs} as determined by FIDA increases with P_{STED} (figure 2(b)), which confirms its inappropriate use. Slight deviations between N_{fcs} determined by FCS and FIDA may result from experimental differences between the two techniques as described in the discussion following equation (12). The adapted system parameters a_0 , a_1 and a_2 varied with P_{STED} , indicating a change of the fluorescence detection profile $h(r)$. While this change is in principle to be expected from the confinement of $h(r)$ by STED, the values of a_0 , a_1 and a_2 reveal an increase of volume fractions with low brightness. This is visualized by using the values of a_0 , a_1 and a_2 to calculate (equation (6)) the relative volume size $V(h)$ a relative brightness h spans (figure 3(a)). For comparison of $V(h)$ at different P_{STED} , we applied an arbitrary normalization $V = 1$ at $h = 5 \times 10^{-5}$. The increasing low-brightness contributions result in an increase of the detection volume V_{fcs} as determined by equation (3), rendering the increase of $N_{\text{fcs}} (\sim V_{\text{fcs}})$ and the vast decrease of the fluorescence brightness q ($\sim 1/V_{\text{fcs}}$, section 2.7) from ≈ 70 kHz down to ≈ 7 kHz (figure 3(b)). Both N_{fcs} and q are determined by fluorescence signal emitted from all parts of the detection volume, i.e. also from low-brightness volume shells as depicted in the theoretical section 2.8.

The actual detection volume V (equation (5)) and particle number $N = cV$ may be a more accurate measure of our experimental conditions, since they do not overweigh low brightness contributions. However, experimental determination of N requires the calculation of the scaling factor γ (equation (9)), whose exact determination is difficult when reducing the detection volume by STED. Therefore, we estimated values of N by applying a modified FIDA approach (section 2.8). Instead of varying the system parameters a_0 , a_1 and a_2 , we determined values of a_0 , a_1 and a_2 at diffraction-limited conditions, which feature the brightness–volume relation of a rather compact fluorescence detection profile $h(r)$, and fixed these values throughout further analysis resulting in values of an apparent particle number N^* , an apparent fluorescence brightness q^* that is proportional to the focal peak brightness Q_0 , and an apparent low-brightness signal B_b^* (equation (10)). Figure 2(c) shows the dependence of N^* on P_{STED} . For comparison, we again plotted the dependence of τ_{xy} of the FCS analysis and normalized all data on the respective value at zero STED power, i.e. for the diffraction-limited confocal case. τ_{xy} and N^* decrease equally confirming the confinement of the effective focal volume by STED. Further, we observed a strong increase of apparent low-brightness contribution B_b^* up to values of $\approx 65\text{--}70\%$ of the total signal for $P_{\text{STED}} > 100\text{ mW}$ (figure 3(b)). Besides scattering background signal, B_b^* comprises all signal of low fluorescence brightness that is not covered by the underlying brightness–volume relation. Since we kept the system parameters constant, i.e. we apparently regarded a wrong brightness–volume relation with increasing P_{STED} , the increased portion of apparent low-brightness signal B_b^* confirms that the focal confinement by STED introduces an increase of volume fractions of low brightness. The apparent background signal B_b^* further allows us to estimate an apparent particle number N^* from the FCS analysis. Using the values of B_b^* determined by FIDA, we can calculate N^* from the amplitude $G_N(0)$ of the correlation function (equation (11)). The, in this way, determined decrease of N^* coincides with that observed of τ_{xy} and of N^* from FIDA (figure 2(c)).

Increasing contributions of apparent low brightness signal are further confirmed by the dependence of the apparent fluorescence brightness q^* (figure 3(b)) and scaling factor γ (figure 3(c)) on P_{STED} . The decrease of q^* follows that of the focal peak brightness Q_0 (compare section 2.8) and is much less pronounced than the decrease of q . (We will discuss reasons of a general decrease of the fluorescence brightness further below). The scaling factor γ quantifies the compactness of the fluorescence detection profile $h(r)$ (equation (4)): compact (near rectangular) profiles give values of γ close to one, while values of $\gamma \ll 1$ characterize profiles with large volume contributions of low brightness. As outlined before, we lack exact knowledge of $h(r)$ and thus cannot properly calculate γ . However, we can estimate relative changes of γ with STED confinement by the proportionality to the ratio N^*/N_{fcs} (equation (11)). As expected, γ declines with focal confinement by STED.

We have used information from FIDA to correct FCS analysis for a proper determination of the particle number. An optimized analysis introduces global fitting of correlation and photon histogram data, applying N^* , the lateral diffusion time τ_{xy} , the fluorescence brightness q^* and the apparent background signal B_b^* as global parameters common to both correlation and histogram evaluation. The global FCS–FIDA analysis fits the correlation and FIDA data well (figure 2(d)) and is outlined in the appendix in detail. The values of N^* , τ_{xy} , q^* or B_b^* determined by the global FCS–FIDA analysis coincide with those determined by single FCS and FIDA analysis (figure 2(c)).

The increasing contributions of apparent low-brightness signal damp the signal-to-noise ratio and thus the general performance of our single-molecule studies. For example, FCS data

recorded for $P_{\text{STED}} = 50 \text{ mW}$ are more noisy than those recorded without STED (compare figure 2(a)). The lower signal-to-noise ratio is also due to a decrease of the focal peak fluorescence brightness as revealed by q^* (figure 3(b)). The decrease of brightness most probably stemmed from residual intensity in the center of the doughnut-shaped STED focus most properly due to imperfections of the optical imaging setup. Such imperfections may also result in an anisotropic intensity distribution of the doughnut-like STED focus, deteriorating the focal confinement by STED. From our calibration measurements (figure 1(b)), we would assume a reduction of the focal diameter by a factor of 5–6 for $P_{\text{STED}} = 180 \text{ mW}$, which is 1.5–1.8-fold larger than the factor of ~ 3.3 , which we determined for our measurements in aqueous solution. Optical imperfections may result from distortions of the wavefront or polarization at optical parts such as lenses or (dichroic) mirrors or from the refractive index mismatch of the employed $\text{NA} = 1.42$ oil immersion objective and the aqueous sample. Such optical imperfections disclose no principle limits of nanoscale STED microscopy, since they can be corrected for if necessary. In our experiments, we minimized the contributions from the refractive index mismatch by measuring less than $5 \mu\text{m}$ inside the aqueous solution [36]. Setting up a water immersion objective, which avoids such refractive index mismatch, is possible for nanoscale single-molecule spectroscopy (see figure 6), but due to its lower NA (usually 1.2) results in a larger focal volume from the very start (compare equation (19)).

3.3. Dependence on experimental conditions

3.3.1. Adaptation of the refractive index. To check for the influence of the refractive index mismatch on the performance of our STED–FCS/FIDA measurements, we applied TDE as an environment for single-molecule dynamical studies at the nanoscale. The refractive index of TDE of $n \approx 1.51$ – 1.52 matches that of the immersion oil ($n = 1.52$) and should minimize optical imperfections. TDE has previously been successfully applied in microscopy applications relying on proper phase adjustment [37]. Compared to water, TDE is characterized by an increased viscosity and thus slower molecular diffusion. Further, the fluorescence brightness of Atto647N is a factor of 3 worse in TDE than in water. The different polarity as well as the lower mobility of molecular oxygen leads to a reduced fluorescence quantum yield and a larger triplet population in TDE. Similar to the measurements in aqueous solution, we recorded FCS and FIDA data for increasing power P_{STED} of the STED light for Atto647N in TDE.

Figure 4(a) shows the dependence of the particle number as a measure of the focal confinement by STED in TDE. Following the results of our experiments in water, we determined values of two types of particle numbers: N_{fcs} determined by FCS (equation (3)) and the apparent particle number N^* determined by FIDA (equation (10)). We applied different focal shapes of the STED light. For comparison, let us at first behold the values recovered for the same lateral xy -doughnut-shaped STED intensity distribution as we have used for the previous measurements in water. Similar to the particle numbers determined in water, the values of N_{fcs} increase with P_{STED} while those of N^* decrease. The decrease of N^* is again in accordance to the decrease observed for the lateral diffusion time τ_{xy} (which decreases from 1.2 ms down to $55 \mu\text{s}$ at $P_{\text{STED}} = 180 \text{ mW}$, data not shown). The adaptation of the refractive index brings along one major advantage: at the same STED power $P_{\text{STED}} = 180 \text{ mW}$, the ~ 5 -fold confinement in focal diameter is much better than the factor of ~ 3.3 in water and almost matches the 5–6-fold confinement expected from calibration (figure 1(b)). Some optical imperfections obviously remain, resulting in an insufficient intensity zero of the STED doughnut as witnessed

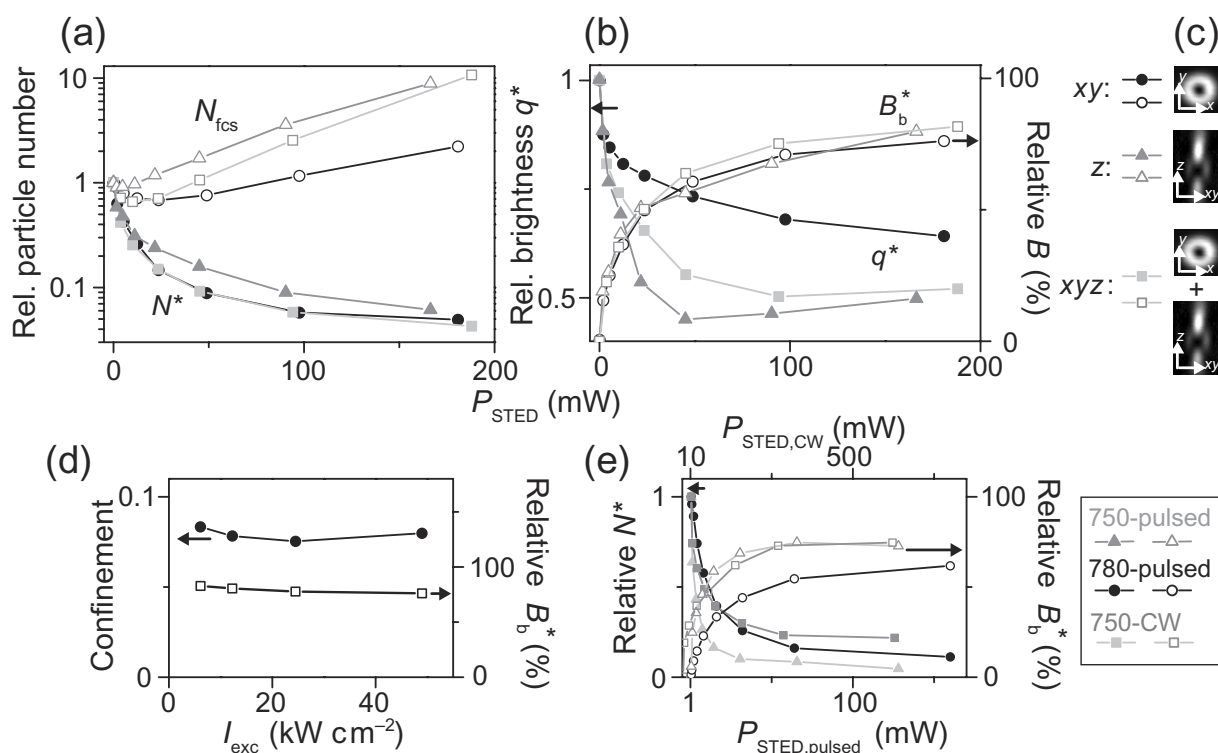


Figure 4. STED-FCS/FIDA of the dye Atto647N in TDE with different modes of focal confinement by STED. (a) Relative dependence of the particle numbers N_{fcs} (open symbols) and N^* (closed symbols) on the STED power P_{STED} (780 nm) determined by FCS and FIDA, respectively, for different focal engineered spots of the STED light: lateral xy - (black circles), axial z - (grey triangles), and 3D xyz -confinement (light grey squares). (b) Relative dependence of the apparent fluorescence brightness q^* (closed symbols) and of the relative fraction of apparent low-brightness background B_b^* (open symbols) on P_{STED} for the different modes of focal confinement. (c) Focal intensity distribution of the STED light for the lateral xy - and axial z -confinement. The 3D xyz -confinement is an addition of both. (d) Dependence of the focal confinement by STED ($\text{Confinement} = \tau_{xy}(\text{STED})/\tau_{xy}(\text{confocal})$, closed circles) and apparent background contribution B_b^* (open squares) at STED recording ($P_{\text{STED}}(780 \text{ nm}) = 180 \text{ mW}$, xy -confinement) on the excitation intensity I_{exc} . (e) Dependence of the apparent particle number N^* (closed symbols, normalized to $P_{\text{STED}} = 0$) and apparent background contribution B_b^* (open symbols) on the STED power P_{STED} for pulsed STED light at 780 nm (circles) and 750 nm (grey triangles) and for CW STED light at 750 nm (grey squares).

by a decrease of the fluorescence brightness q^* down to $\sim 65\%$ of its initial value (figure 4(b)), which is less compared to the 2-fold decrease in water but still notable. As before, the focal confinement by STED gives rise to an increasing contribution of up to 65–70% of apparent low-brightness signal B_b^* (figure 4(b)), resulting in the characteristic increase of N_{fcs} and thus a bit more noisy single-molecule data at large P_{STED} .

3.3.2. Modus of confinement. Besides the xy -doughnut-shaped STED intensity distribution, figure 4(a) also shows the dependence of N_{fcs} and N^* on the focal confinement for other STED foci: z -confinement, i.e. intensity distribution of the STED light primarily confining the focal volume along the axial z -direction, and xyz -confinement realized by overlaying the engineered foci for the xy - and the z -confinement (figure 4(c)). In all cases, we observed a similar behavior (figures 4(a) and (b)): a decrease of N^* due to the confinement in fluorescence detection volume, an increase of N_{fcs} due to an increased contribution of apparent low-brightness signal B_{b}^* , and a decrease of the fluorescence brightness q^* , overall establishing somewhat more noisy fluctuation data. Yet, slight differences arise from the different modes of focal confinement: (i) quenching of the fluorescence brightness q^* is weakest for the xy - (down to 65%), and strongest for the z -confinement (down to 50%). Most probably the residual intensity in the center of the engineered STED foci is larger for the z -confinement. (ii) The reduction of the detection volume by STED at $P_{\text{STED}} = 180$ mW is largest for the xyz -confinement (25-fold) and lowest for the sole z -confinement (15-fold). While we *per se* expect the strongest reduction for the confinement along all spatial directions, the rather bad performance of the z -confinement has several reasons. First, focal confinement is predominantly only 1D. Further, the intensity maxima of the focal STED light distribution of the z -confinement are further apart than of the xy -doughnut (figure 4(c)), demanding for larger powers P_{STED} to realize the same focal volume reduction [34].

Further, we have performed STED–FCS and STED–FIDA at other experimental conditions. We observed an increased apparent low-brightness contribution regardless of the choice of excitation light intensity, STED wavelength, or modus of fluorescence state inhibition by pulsed or CW STED light. Irrespective of increasing the excitation intensity I_{exc} from 5 to 50 kW cm⁻², xy -confinement with $P_{\text{STED}} = 130$ mW at 780 nm yielded similar reductions of detection volume and the same contributions of ~ 65 –70% of apparent low-brightness signal (figure 4(d)). Further, we did not observe a significant improvement in volume confinement or a reduction of apparent low-brightness contributions when changing the wavelength of the STED light from 780 to 750 nm (figure 4(e)). Compared to 780 nm, the STED wavelength of 750 nm is closer to the emission maximum of ~ 670 nm of the Atto647N dye in aqueous solution, resulting in an increased efficiency of stimulated emission [38] and thus providing a steeper decline of the focal confinement with P_{STED} . However, 750 nm is also closer to the absorption maximum of ~ 645 nm of the Atto647N dye in aqueous solution, yielding an increased probability of anti-Stokes fluorescence excitation and thus a larger apparent low-brightness signal contribution B_{b}^* . Finally, it has been shown that nanoscale STED microscopy is not implicitly restricted to pulsed, but can also be realized with CW excitation and STED light, which simplifies laser sources needed [39]. The study of single-molecule dynamics in reduced focal volumes formed by the CW STED approach is possible (figure 4(e)). Compared to pulsed STED we had to apply $(\ln 2 f \tau_{\text{F}})^{-1} = 5$ -fold more average power P_{STED} of the STED light where $f = 76$ MHz is the repetition rate of the pulsed mode and $\tau_{\text{F}} = 3.8$ ns the fluorescence lifetime of Atto647N in TDE. Although resulting in a similar fraction B_{b}^* , the performance of our ‘CW-mode’ measurements turned out to be slightly worse than the ‘pulsed-mode’ measurements because we obtained less confinement of the focal volume at comparable P_{STED} . A possible reason may be residual fluctuations of the power level of the CW STED light source.

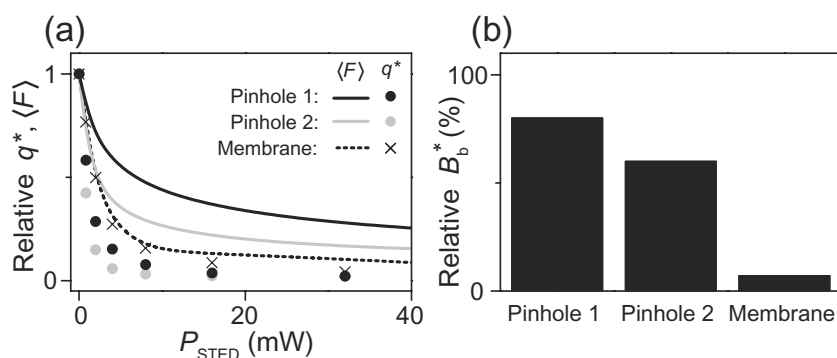


Figure 5. Characteristics of apparent low-brightness background contribution. (a) Fluorescence switch-off by the STED light depicted as the relative decrease of the apparent fluorescence brightness q^* (circles) and ensemble count-rate $\langle F \rangle$ (lines) of Atto647N fluorescence in TDE with increasing power P_{STED} of the STED light (780 nm) as determined by FIDA. Switch-off of q^* is complete; the difference to the total signal $\langle F \rangle$ stems from apparent low-brightness signal contribution and decreases with the size of the confocal pinhole (pinhole 1 (black) $1.4\times$ and pinhole 2 (grey) $0.8\times$ the magnified Airy-disc of the confocal spot) and almost diminishes in measurements of Atto647N-PE incorporated in a multilamellar membrane sheet (q^* : cross, $\langle F \rangle$: dotted line). (b) The contribution of apparent background signal B_b^* of the STED-FCS/FIDA experiments of Atto647N in TDE decreases with the size of the confocal pinhole (pinhole sizes as in (a)), and almost diminishes in measurements of Atto647N-PE incorporated in a multilamellar membrane sheet ('membrane'). B_b^* is caused by incomplete fluorescence switch-off from axial out-of-focus areas. While fluorescence state inhibition in (a) was measured with a non-engineered focal spot of STED light, we applied the doughnut-shaped intensity distribution of the STED light in (b).

3.4. Suppression of low-brightness signal contributions

Several reasons might be responsible for the occurrence of the large contributions of apparent low-brightness signal. We can exclude significant contributions from scattering signal of the excitation or STED light or from fluorescence excitation by the STED light via one-, two- or multi-photon absorption. For both excitation and STED light, the count rates observed from a purely scattering sample such as the pure solvent and the signal detected from the fluorescence samples for the STED light alone were much less than the apparent background signal $B_b^* > 10$ kHz obtained in our STED-FCS/FIDA experiments. Furthermore, we did not observe scattering signal contributions in the fluorescence lifetime data recorded by time-correlated single-photon counting for increasing P_{STED} . The fluorescence lifetime determined from the residual signal of the measurements at large P_{STED} revealed the values of 3.4 and 3.8 ns of Atto647N in water or TDE, respectively.

On a single-molecule level, switch-off of fluorescence by stimulated emission was almost complete as shown in figure 5(a). We overlaid the excitation spot with a slightly larger non-engineered focus of the STED light at 780 nm and recorded FIDA data for increasing STED power P_{STED} . In this way, we sampled the degree of fluorescence state inhibition by stimulated

emission by determining the (apparent) brightness q^* . While q^* declined to almost zero kHz ($<5\%$ compared to its initial value) for $P_{\text{STED}} > 10$ mW, the detected ensemble count-rate $\langle F \rangle$ showed residual levels of $>15\%$. FIDA theory can explain this discrepancy between q^* and $\langle F \rangle$ only from apparent background signal B_b^* (equation (10)). Importantly, we could minimize this discrepancy by applying smaller diameters of the confocal detection pinhole (figure 5(a)). We thus analyzed the correlation between pinhole diameter and contribution of apparent background signal also in our focal-confinement STED–FCS/FIDA experiments applying the doughnut-like intensity distribution of STED light (figure 5(b)). Smaller pinholes resulted in decreasing apparent background signal, and because reducing the pinhole size reduces the relative contribution of out-of-focus planes we can conclude that the apparent low-brightness contributions originate from these areas where fluorescence state inhibition by STED is not effective.

Unfortunately, smaller confocal detection pinholes also reduce the detection efficiency of signal from the focal plane and consequently the sensitivity of our single-molecule based measurements. With the corrections outlined above in place, there will therefore be an optimal pinhole size resulting in the best signal-to-noise ratio for every given degree of confinement. Nevertheless, unless otherwise addressed, the effect of axial out-of-focus contributions will ultimately put a lower limit on the focal volumes achievable in 3D with STED.

This finding makes application of STED confinement to systems that inherently lack any out-of-focus contributions all the more interesting. The 2D samples such as lipid membranes should therefore feature excellent signal-to-noise ratios at very high levels of confinement, and indeed, single-molecule data recorded for an Atto647N-labeled phosphoglycerolipid (Atto647N-PE), which we introduced into a multilamellar (phosphoglycerolipid) membrane layer, revealed proper fluorescence switch-off by STED and hardly any low-brightness contributions (figure 5).

3.5. STED–FCS on lipid membranes

Figure 6 shows the results of the analysis of the FCS and FIDA data recorded for the fluorescent phosphoglycerolipid Atto647N-PE in a multilamellar lipid membrane layer. We employed the xy -doughnut-shaped engineered focus of the STED light and positioned the centers of the overlaid excitation and STED spot on the membrane layer. With increasing power P_{STED} and thus increasing confinement of the focal area, the correlation data show both the expected decrease of the transit time τ_{xy} and the increase of the amplitude $G_N(t_c)$ (figure 6(a)). The correlation data recorded on the membrane layer for $P_{\text{STED}} = 50$ mW was less noisy than that recorded in aqueous solution (compare figure 2(a)). The membrane layer precludes diffusion along the axial direction. Therefore, we fitted the correlation data with the 2D diffusion model (equation (13), $\alpha = 1$). The transit time τ_{xy} and the particle numbers N_{fcs} and N^* as determined by FCS and FIDA consistently evidence a >25 -fold confinement of the focal spot at $P_{\text{STED}} = 180$ mW from a diffraction-limited diameter of ~ 240 nm down to ~ 40 – 50 nm (figure 6(b)). This 5–6-fold decrease in focal diameter is as expected from calibration (figure 1(b)). Our measurements on 2D samples such as membranes thus showed hardly any influence by optical imperfections and as expected from the previous results of figure 5 the influence of apparent low-brightness noise from axial out-of focus regions was negligible: the fraction of apparent low-brightness signal B_b^* determined by FIDA was $<5\%$. Since $N_{\text{fcs}} \sim N^*$, we will further on just denote a particle number N for the measurements on membranes. The single-molecule fluorescence traces observed in the nanoscale foci show signal-to-noise ratios larger than 100

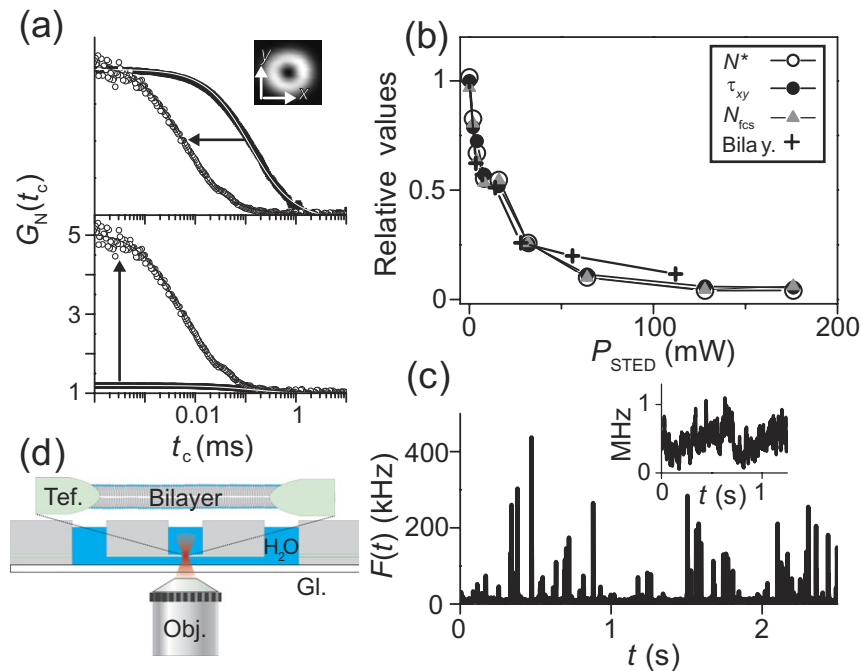


Figure 6. STED–FCS/FIDA on lipid membranes. (a) Correlation data $G_N(t_c)$ of Atto647N-PE in a multilamellar lipid membrane layer at confocal (black circles) and STED recording (open circles) with $P_{\text{STED}} = 50$ mW (780 nm) and the doughnut-shaped intensity distribution together with fits (grey lines) of equation (2) to the data: normalization at $t_c = 0.001$ ms (upper panel) and original data (lower panel), showing a decrease of the decay time along with a rise of the amplitude upon focal confinement (arrows). (b) Relative dependence of the transit time τ_{xy} (black circles), the particle numbers N_{fcs} (grey triangles) and N^* (open circles) on the STED power P_{STED} along with the relative decrease of τ_{xy} from the measurement on the horizontal membrane bilayers applying a water immersion objective (cross, ‘Bilay.’). (c) Fluorescence count-rate $\langle F(t) \rangle$ of single Atto647N-PE lipids diffusing in a multilamellar membrane layer recorded in consecutive time windows of 1ms with $P_{\text{STED}} = 170$ mW, and concomitant confocal ($P_{\text{STED}} = 0$ mW) recording (inset). (d) Scheme of the setup used for the horizontal black lipid membrane bilayers with microscope objective (Obj.), microscope cover glass (Gl.), focal laser spot (red), lipid membrane bilayer, Teflon support (Tef.) and aqueous solution (H_2O). The distance between cover glass and bilayer and thus focus was >100 μm .

(figure 6(c)) and outline the excellent ability of performing single-molecule based experiments in STED microscopy. Further, these measurements depict how STED microscopy enlarges the practical range of fluorophore concentration for single-molecule detection. While fluorescence bursts from single-molecule transits were clearly observable in the STED recording, the increased number of particles in the larger detection volume of the confocal recording did not allow direct distinguishing of single-molecule events at the same concentration of fluorescent molecules (inset figure 6(c)). In this way, single-molecule experiments can be performed at larger, sometimes endogenous and inevitable concentrations.

Our nanoscale observations on membranes not necessarily require the use of an oil-immersion objective with lipid membranes arranged close to the microscope cover glass. We have also succeeded to perform FCS and FIDA experiments in reduced focal areas formed by STED microscopy applying an $NA = 1.2$ water immersion objective lens (figure 6(b)). In these experiments, we measured the diffusion of the Atto647N-PE in horizontal membrane (black lipid) bilayers formed across microholes approximately $100\text{--}150\ \mu\text{m}$ above the cover glass (figure 6(d)). Again, the apparent background contribution determined by FIDA was negligible and stayed constant with P_{STED} , optimizing signal-to-noise ratios and minimizing bias of the FCS analysis. Measuring on such horizontal lipid bilayers not only outlines the possibility to monitor single-molecule dynamics at the nanoscale inside cells or tissues but also to combine this technique with other readouts such as electrophysiological recordings [21, 22].

3.6. Photobleaching

The large intensities of STED light may lead to additional photobleaching [19]. However, photobleaching has minor influence on our dynamical measurements. As plotted in figure 7(a) for measurements on the multilamellar membranes, the decline of both τ_{xy} and N scaled with the dynamical reduction of the focal area $A \sim r_{xy}^2$ by STED. This linear dependence is expected from theory, since $N \sim A$ and $\tau_{xy} \sim r_{xy}^2$ for the free diffusion of Atto647N-PE in the multilamellar membrane, and confirms that the reduction of τ_{xy} and N stemmed from the STED confinement, and not from other light-induced characteristics such as photobleaching.

Further, photodestruction following the pure excitation process was hardly observed in the reduced focal areas compared to the confocal case, as depicted in figure 7(b) for our multilamellar measurements. Starting at $\sim 10\ \text{ms}$ at low excitation intensity I_{exc} , τ_{xy} decreased with I_{exc} by a factor of two at $I_{\text{exc}} = 480\ \text{kW cm}^{-2}$ due to photobleaching for confocal detection. In contrast, we hardly observed a decrease of τ_{xy} with I_{exc} for STED microscopy at $P_{\text{STED}} = 160\ \text{mW}$. This low influence by photobleaching follows from important geometrical characteristics of the STED approach. The molecular transit times through the nanoscopic volumes are much shorter than for confocal recording, i.e. the time span of probable photobleaching during non-switched-off fluorescence emission is pushed down significantly [40]. Photobleaching may however effect FCS measurements on molecules featuring hindered diffusion due to, for example, trapping on the nanoscale. In this case, the focal transit time does not scale with the focal diameter and molecules may also dwell longer in the reduced focal spots [31]. Here, photobleaching may be minimized by scanning of the beam [41, 42].

Photodestruction may be enhanced during the passage through the ‘fluorescence switch-off’ area of STED light. In this case, the number of particles reaching the focal center might be cut down. However, at our experimental conditions we have not observed a significant decrease in the particle number other than stemming from the focal confinement by STED (figure 7(a)). Most importantly, while ‘dilution’ of fluorescent particles by STED photobleaching may bias concentration measurements it is of minor importance for the analysis of dynamics on the nanoscale: as long as some molecules reach the focal center undestroyed, their dynamics are unaltered and can be studied.

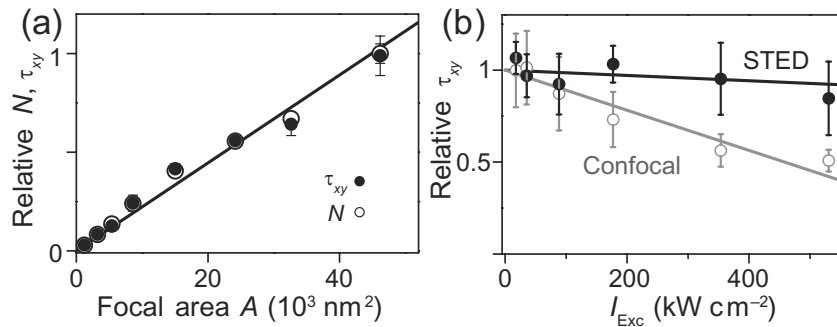


Figure 7. Influence of photobleaching on STED-FCS/FIDA. (a) Relative reduction of the particle number $N(=N^*)$ (open circles) and average transit time τ_{xy} (closed circles) of Atto647N-PE in multilamellar membrane layers with focal area $A = \pi r_{xy}^2$ confined by STED. All values are normalized to the value determined with the confocal spot. As expected from an ‘ideal’ reduction of the fluorescence spot by STED, N and τ_{xy} decline in proportion to the focal area, according to free diffusion of the lipids (straight line). This characteristic is a strong argument against STED light-induced effects other than the spot size reduction. The values of the lateral radius r_{xy} were determined from the calibration measurements of figure 1(b). (b) Relative decrease of the average transit time τ_{xy} of Atto647N-PE diffusion in multilamellar membrane layers with excitation intensity I_{exc} for confocal (open circles) and STED recording (closed circles, $P_{\text{STED}} = 160 \text{ mW}$). While τ_{xy} is reduced down to $\sim 50\%$ due to photobleaching at confocal recording, photobleaching by the excitation light is negligible for STED recording.

3.7. Live cell observations

Figure 8 shows results of our FCS experiments on Atto647N-labeled phospholipid PE (phosphoethanolamine) and Atto647N-labeled sphingolipid SM (sphingomyelin) inserted into the plasma membrane of living PtK2 cells. The fluorescence fluctuations of the single lipid transits exhibited diffusion times τ_{xy} with continuously decreased area $A \sim r_{xy}^2$ of the focal spot (figure 8(a)). We dynamically reduced A approximately 70-fold from a diffraction-limited diameter of 250 nm down to 30 nm by gradually increasing P_{STED} (we estimated the values of A from the radii determined in figure 1(b)). A linear dependence of τ_{xy} on A indicates free diffusion (compare equation (13) $\tau_{xy} \sim r_{xy}^2/D$) as exemplified in figure 8(a) for a diffusion constant $D = 5 \times 10^{-9} \text{ cm}^2 \text{ s}^{-1}$ (grey dotted line). Atto647N-labeled PE almost diffuses freely and only shows slight deviation from the linear behavior for small focal spots. Deviation from linear behavior is much more pronounced for the Atto647N-labeled sphingolipid SM, a clear indication of anomalous diffusion [31]. Diffusion of the labeled lipids is slower and deviates from free diffusion especially when measuring with small focal spots. This indicates that upon tuning the observation area to small sizes we reach the scale of the heterogeneities causing the anomalous diffusion and resulting in the strong deviation of $\tau_{xy}(A)$ from a linear dependence on A . STED microscopy thus uniquely can distinguish anomalous from free diffusion on these length scales.

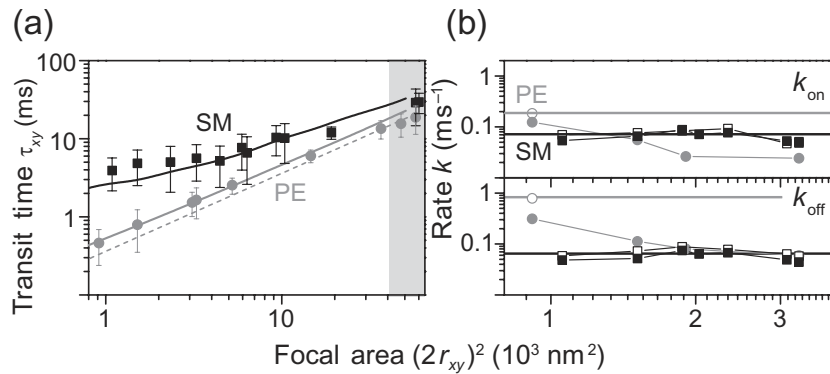


Figure 8. STED–FCS of lipid diffusion in the plasma membrane of living PtK2 cells. (a) Transit time τ_{xy} of Atto647N-labeled PE (grey circles) and SM (black squares) determined from fitting equation (13) to the experimental data recorded for focal spots of radius r_{xy} continuously downscaled by STED; error bars result from averaging over more than 30 FCS measurements on different cells. A comparison to the linear decrease with the focal area $A \sim r_{xy}^2$ (grey dotted line) confirms nearly free diffusion for PE and pronounced hindered diffusion of SM, but not for the confocal recordings (grey shaded area). The experimental data of PE and SM can be described consistently by Monte Carlo simulated data including transient binding with on and off rates $k_{\text{on}} = 190 \text{ s}^{-1}$, $k_{\text{off}} = 800 \text{ s}^{-1}$ (grey line) and $k_{\text{on}} = k_{\text{off}} = 80 \text{ s}^{-1}$ (black line), respectively. The values of the lateral radius r_{xy} were determined from the calibration measurements of figure 1(b). (b) On rate k_{on} (upper panel) and offrate k_{off} (lower panel) for transient binding of PE (grey circles) and SM (black squares) determined from fitting equation (14) (closed symbols) or equation (15) (open symbols) to the experimental data. The black and grey lines approximate the resulting values of k_{on} and k_{off} , which can only be reliably determined for the STED ($r_{xy} < 70 \text{ nm}$).

Our observation of heterogeneous lipid diffusion is consistent with previous FCS measurements, where similar characteristics have been observed for sphingolipids either by extrapolating the dependence of τ_{xy} on A as measured for diffraction-limited and larger foci to the nanoscale [10] or measuring $\tau_{xy}(A)$ on the plasma membrane of cells grown over 100–200 nm large nanoapertures, mechanically confining the focal area [11]. However, our far-field measurements at the length scales of interest deliver much more reliable and more model-independent results about the nanoscopic details of lipid dynamics, since they allow direct and least invasive determination of the origin of the anomaly in diffusion. Our previous STED–FCS measurements of lipid diffusion have already revealed transient, cholesterol-assisted complexes of nanoscopic dimensions of the sphingolipids with other membrane components [31]. Here, we extend these studies and apply a more detailed analysis of the correlation data allowing for the direct determination of the binding and release rates at these complexes. Figure 8(b) shows the results of fitting equation (14) or (15) to the correlation data, which considers the binding with on- and off-rate constants k_{on} and k_{off} , respectively, to an immobile partner in the diffusion path of the molecule. Reliable results of this fitting procedure have only been obtained for the correlation data recorded for focal spots of diameter ($2r_{xy}$) $< 70 \text{ nm}$ rendering

$k_{\text{on}} \approx k_{\text{off}} \approx 80 \text{ s}^{-1}$, i.e. an equilibrium constant $K = k_{\text{on}}/k_{\text{off}} \approx 1$ for SM. The off rate coincides well with the trapping duration of $\sim 10 \text{ ms}$ estimated in our previous analysis [31], and Monte Carlo simulations of lipid membrane diffusion (section 3.1) for $k_{\text{on}} \approx k_{\text{off}} \approx 80 \text{ s}^{-1}$ result in a consistent description of the focal area dependence of $\tau_{xy}(A)$ (figure 8(a)). The coinciding values of k_{on} and k_{off} determined from the reaction-dominated (equation (14)) and precise model (equation (15)) confirm that only by downscaling the focal radius r_{xy} we ensure that a freely diffusing molecule spends only little time τ_{free} in the detection area reaching the experimental condition that diffusion is dominated by trapping: $1/k_{\text{off}} \gg \tau_{\text{free}} \sim r_{xy}^2$.

We can now even quantify the slight deviation from normal diffusion of PE. While the reaction-dominated model (equation (14)) does not give congruent results even for $r_{xy} = 15 \text{ nm}$, the precise model (equation (15)) renders on and off rates $k_{\text{on}} \approx 190 \text{ s}^{-1}$ and $k_{\text{off}} \approx 800 \text{ s}^{-1}$ (figure 8(b)). Monte Carlo simulations with these rates give a consistent description of the experimentally observed dependence of $\tau_{xy}(A)$ (figure 8(a)). With $1/k_{\text{off}} = 1.25 \text{ ms}$ and $\tau_{\text{free}} \approx 0.5\text{--}1.5 \text{ ms}$ diffusion of PE is not reaction-dominated for $r_{xy} > 15 \text{ nm}$ and the reaction-dominated model consequently fails. In comparison to SM, k_{on} is 2-fold larger, but the 10-fold larger off rate establishes a much less pronounced trapping and thus results in the almost normal free diffusion of PE [31].

We have assumed a free diffusion coefficient $D_{\text{free}} = 5 \times 10^{-9} \text{ cm}^2 \text{ s}^{-1}$ of the lipids in our analysis as estimated from the confocal data and known from previous results [31]. The results do not significantly change when assuming slightly different values of D_{free} . For example, changing fixed values of D_{free} from 4 to $6 \times 10^{-9} \text{ cm}^2 \text{ s}^{-1}$ results in $k_{\text{on}} \approx k_{\text{off}} \approx 65\text{--}90 \text{ s}^{-1}$. Fitting equation (15) to the data (for $r_{xy} < 20 \text{ nm}$) with D_{free} as an additional free parameter yields $D_{\text{free}} \approx 4 \times 10^{-9} \text{ cm}^2 \text{ s}^{-1}$ and $k_{\text{on}} \approx k_{\text{off}} \approx 65 \text{ s}^{-1}$, however, with a large variance $\approx 60\%$.

Most strikingly, only the $< 70 \text{ nm}$ large spots of the STED microscope can reveal the observed details of lipid membrane dynamics, simple confocal data render normal diffusion for both SM and PE with a slightly lower diffusion coefficient in the case of SM [31]. The demonstrated hindered diffusion of the lipids in the plasma membrane of living cells highlights the great potential of STED microscopy to address prominent biological problems such as details on the formation of lipid membrane organization (lipid ‘rafts’).

4. Conclusion

Using STED microscopy we have shown the far-field fluorescence observation of single-molecule dynamics in focal volumes of down to 30 nm in diameter. Even smaller volumes will be available with optimized instrumentations. The signal-to-noise ratio of the nanoscale experiments in 3D, open volumes was influenced by contributions of low-brightness signal from axial out-of-focus areas but can be corrected at the cost of lower signal-to-noise ratios. In contrast, single-molecule data recorded on 2D samples such as membranes provided excellent signal-to-noise ratios similar to those of confocal recordings. Being non-invasive, far-field studies of single-molecule dynamics at the nanoscale open the way to a whole field of new experiments. With observation volumes reaching the macromolecular scale, details of molecular motion can now be revealed with higher sensitivity. This allows us to address important questions about the nano-organization of molecules, prominently the details of hindered diffusion of molecules in the plasma membrane of living cells and their organization into nanodomains [31]. Specifically, we showed here that STED microscopy uniquely determines binding and release rates of nanoscale lipid interactions. Alternative far-field optical nanoscopy

techniques based on stochastic switching and mathematical localization of single molecules are equally powerful in resolution [43, 44], but by electing random molecular events within a $d > 300$ nm detection area, they lack the ability to probe within a specific subdiffraction site. A further advantage of the STED approach is that the focal spot can be dynamically tuned in a controlled manner. Following the dependence of molecular transit times on the focal spot size or shape down to the nanoscale provides additional information on the characteristics of molecular dynamics such as local trapping or directional flow. Further on, with the smaller detection foci formed in STED microscopy the range of single-molecule based experiments can easily be expanded to cases where larger, sometimes endogenous concentrations are inevitable.

Sufficient signal levels for single-molecule measurements in STED microscopy are also realizable with different modes of experimental design such as 2D or 3D focal confinement, continuous or pulsed laser light, and $> 100 \mu\text{m}$ away from the cover glass in solution, which provides nanoscale observations inside living cells or tissues. Compared to confocal recording, the diffusion time in the nanoscopic volumes formed by STED is strongly reduced and the effect of photobleaching on freely traversing molecules is thus reduced.

Combinations of STED–FCS with total-internal-reflection [45, 46], multi-photon excitation [47] or with 4Pi microscopy [48] may further reduce the noise from axial out-of-focus areas, especially in cellular measurements with significant background due to autofluorescent or internalized molecules. Also, scanning of the beam may further increase the sensitivity of the STED–FCS measurements and allow for combining nanoscale spatial and temporal information [41, 42]. Nanoscopic focal spots may also be formed by fluorescence switching processes other than STED, such as reversible photoswitchable fluorophores or dark state transitions [17, 49]. In addition to the tuning of the detection volume as described above, photoswitching can also be used to tune the number of visible fluorophores and thus to optimize the signal-to-noise ratio for varying given concentrations of markers [50]. Last but not least, one could combine different fluorescence and physical readouts on the nanoscale, such as simultaneous recording of fluorescence intensity, lifetime, anisotropy and color together with temperature, force or electrical currents. Overall, we expect the ability to perform single-molecule studies at the nanoscale to be important for tackling many outstanding problems in all scientific areas where nano-organization is the key to the functionality.

Acknowledgments

We thank C v Middendorff, L Kastrop, V Belov (Göttingen), and G Schwarzmann (Bonn), P Kask (Tallinn) and H Rigneault (Marseille) for fruitful discussion and M Hilbert (Göttingen) for a critical reading of the manuscript.

Appendix. Global FCS–FIDA analysis

We performed a global FCS–FIDA analysis by fitting simultaneously recorded correlation and PCH data with the same set of parameters, respectively. For the global analysis, we found it more convenient to use the un-normalized correlation function $G(t_c)$, which is directly proportional to the focal peak fluorescence brightness squared Q_0^2 [1]. For FIDA, we applied our heuristic approach resulting in values of N^* , q^* ($\sim Q_0$), and B_b^* . The values of N^* and q^* have to be interconverted between correlation and histogram analysis by taking into account the sampling rate of FIDA, i.e. the ratio of sampling time window ΔT and average transit time τ_{xy} of a single

molecule through the focal area $\Delta T/\tau_{xy}$, as outlined in equation (12). However, instead of calculating S applying equation (12), we found it more reliable to introduce S as an additional fitting parameter [29]. We weighted the individual FCS and FIDA fits by the inverse of the fit function's value [5], and applied an additional fitting parameter that adapts fit-weighting between both analysis methods.

Overall, both the correlation and histogram data were accurately reproduced by using the same set of parameters, as exemplified in figure 2(d). The values of N^* , q^* and τ_{xy} obtained by the global FCS–FIDA analysis coincide with those determined from the individual FIDA and FCS analysis. Further, from the resulting values of the correction factor S we can estimate $a = 0.15 \pm 0.06$ according to equation (12).

References

- [1] Magde D, Elson E L and Webb W W 1972 *Phys. Rev. Lett.* **29** 705–8
- [2] Ehrenberg M and Rigler R 1974 *Chem. Phys.* **4** 390–401
- [3] Hausteiner E and Schwille P 2003 *Methods* **29** 153–66
- [4] Chen Y, Müller J D, So P T C and Gratton E 1999 *Biophys. J.* **77** 553–67
- [5] Kask P, Palo K, Ullmann D and Gall K 1999 *Proc. Natl Acad. Sci. USA* **96** 13756–61
- [6] Abbe E 1873 *Arch. Mikr. Anat.* **9** 413–68
- [7] Levene M J, Korlach J, Turner S W, Foquet M, Craighead H G and Webb W W 2003 *Science* **299** 682–6
- [8] Laurence T A and Weiss S 2003 *Science* **299** 667–8
- [9] Schwille P, Korlach J and Webb W W 1999 *Cytometry* **36** 176–82
- [10] Wawrezinieck L, Rigneault H, Marguet D and Lenne P-F 2005 *Biophys. J.* **89** 4029–42
- [11] Wenger J, Conchonaud F, Dintinger J, Wawrezinieck L, Ebbesen T W, Rigneault H, Marguet D and Lenne P-F 2007 *Biophys. J.* **92** 913–9
- [12] Geerts H, De Brabander M, Nuydens R, Geuens S, Moeremans M, De Mey J R and Hollenbeck P 1987 *Biophys. J.* **52** 775–82
- [13] Sheetz M P, Turney S, Qian H and Elson E L 1989 *Nature* **340** 284–8
- [14] Hell S W and Wichmann J 1994 *Opt. Lett.* **19** 780–2
- [15] Hell S W and Kroug M 1995 *Appl. Phys. B* **60** 495–7
- [16] Dose V 2009 *Europhys. Lett.* **86** 10000
- [17] Hell S W 2007 *Science* **316** 1153–8
- [18] Klar T A, Jakobs S, Dyba M, Egnér A and Hell S W 2000 *Proc. Natl Acad. Sci. USA* **97** 8206–10
- [19] Donnert G, Keller J, Medda R, Andrei M A, Rizzoli S O, Lührmann R, Jahn R, Eggeling C and Hell S W 2006 *Proc. Natl Acad. Sci. USA* **103** 11440–5
- [20] Kastrup L, Blom H, Eggeling C and Hell S W 2005 *Phys. Rev. Lett.* **94** 178104
- [21] Mueller D, Rudin O, Tien H T and Wescott W C 1962 *Nature* **194** 979–80
- [22] Hemmler R, Böse G, Wagner R and Peters R 2005 *Biophys. J.* **88** 4000–7
- [23] Martin O C and Pagano R C 1994 *J. Cell Biol.* **125** 769–81
- [24] Schwarzmann G, Hofmann P, Pütz U and Albrecht B 1995 *J. Biol. Chem.* **270** 21271–6
- [25] Widengren J, Mets Ü and Rigler R 1995 *J. Phys. Chem.* **99** 13368–79
- [26] Kask P, Eggeling C, Palo K, Mets Ü, Cole M and Gall K 2002 Fluorescence intensity distribution analysis (FIDA) and related fluorescence fluctuation techniques: theory and practice *Fluorescence Spectroscopy, Imaging and Probes—New Tools in Chemical, Physical and Life Sciences* ed R Kraayenhof *et al* (Berlin: Springer) pp 153–81
- [27] Qian H and Elson E L 1990 *Proc. Natl Acad. Sci. USA* **87** 5479–83
- [28] Koppel D E 1974 *Phys. Rev. A* **10** 1938–45
- [29] Palo K, Mets Ü, Jäger S, Kask P and Gall K 2000 *Biophys. J.* **79** 2858–66

- [30] Michelman-Ribeiro A, Mazza D, Rosales T, Stasevich T J, Boukari H, Rishi V, Vinson C, Knutson J R and McNally J G 2009 *Biophys. J.* **97** 337–46
- [31] Eggeling C *et al* 2009 *Nature* **457** 1159–63
- [32] Schätzel K, Drewel M and Stimac S 1988 *J. Mod. Opt.* **35** 711–8
- [33] Hell S W 2004 *Phys. Lett. A* **326** 140–5
- [34] Harke B, Keller J, Ullal C K, Westphal V, Schoenle A and Hell S W 2008 *Opt. Express* **16** 4154–62
- [35] Ringemann C, Schönle A, Giske A, von Middendorff C, Hell S W and Eggeling C 2008 *ChemPhysChem.* **9** 612–24
- [36] Hell S, Reiner G, Cremer C and Stelzer E H K 1993 *J. Microsc.* **169** 391–405
- [37] Staudt T, Lang M, Medda R, Engelhardt J and Hell S W 2007 *Microsc. Res. Tech.* **70** 1–9
- [38] Rittweger E, Rankin B R, Westphal V and Hell S W 2007 *Chem. Phys. Lett.* **442** 483–7
- [39] Willig K I, Harke B, Medda R and Hell S W 2007 *Nat. Methods* **4** 915–8
- [40] Eggeling C, Widengren J, Rigler R and Seidel C A M 1998 *Anal. Chem.* **70** 2651–9
- [41] Ruan Q, Cheng M A, Levi M, Gratton E and Mantulin W W 2004 *Biophys. J.* **87** 1260–7
- [42] Ries J and Schwille P 2006 *Biophys. J.* **91** 1915–24
- [43] Betzig E, Patterson G H, Sougrat R, Lindwasser O W, Olenych S, Bonifacino J S, Davidson M W, Lippincott-Schwartz J and Hess H F 2006 *Science* **313** 1642–5
- [44] Rust M J, Bates M and Zhuang X 2006 *Nat. Methods* **3** 793–6
- [45] Thompson N L, Burghardt T P and Axelrod D 1981 *Biophys. J.* **33** 435–54
- [46] Ries J, Ruckstuhl T, Verdes D and Schwille P 2008 *Biophys. J.* **94** 221–9
- [47] Denk W, Strickler J H and Webb W W 1990 *Science* **248** 73–6
- [48] Hell S and Stelzer E H K 1992 *J. Opt. Soc. Am. A* **9** 2159–66
- [49] Hell S W 2003 *Nat. Biotechnol.* **21** 1347–55
- [50] Eggeling C *et al* 2007 *Microsc. Res. Tech.* **70** 1003–9